PAPER

Check for updates

Novel MOF-integrated MXene-magnetite electrochemical platform for effective detection of chloramphenicol

Roxana Paz, [ab] Herlys Viltres, [c] Nishesh Gupta, [d] Carolina Leyva, *[a] Seshasai Srinivasan *[c] and Amin Reza Rajabzadeh *[c]

Chloramphenicol (CAP) contamination in natural waters presents an increasing concern due to its persistence and potential risks to ecosystems and human health. To address this challenge, an electrochemical sensing platform based on a Fe_3O_4@MXene@Fe-BDC composite modified screen-printed carbon electrode was developed and characterized. The hybrid material combines the high electrical conductivity of MXene, the magnetic and catalytic properties of Fe_3O_4, and the adsorption capabilities of the Fe-BDC metal–organic framework, resulting in a synergistic enhancement of sensing performance. Using differential pulse voltammetry, the sensor achieved a broad linear detection range from 1 to 309 μM, a low detection limit of 0.26 μM, and a high sensitivity of 0.95 μA μM^{-1} cm^{-2}. X-ray photoelectron spectroscopy and electrochemical analyses revealed that functional groups such as carboxyl, phenolic, and Fe–O play a central role in CAP recognition through hydrogen bonding, π–π interactions, and metal–oxygen coordination pathways. The sensor also exhibited notable stability, retaining 95.7% of its initial response after 20 days, and performed reliably in complex water samples. These results demonstrate the potential of the Fe_3O_4@MXene@Fe-BDC architecture as an efficient and practical tool for monitoring chloramphenicol in environmental settings.

Environmental significance

The widespread presence of antibiotics such as chloramphenicol in aquatic environments poses a growing threat to ecosystems and public health. Also, it contributes to toxic exposure and the proliferation of antibiotic resistance. Detecting these contaminants at low concentrations within complex water matrices remains challenging using conventional analytical methods, which are often costly and labor-intensive. This study addresses this challenge by developing a robust electrochemical sensing platform based on a hybrid MOF MXene–magnetite composite (Fe_3O_4@MXene@Fe-BDC). The primary finding indicates that integrating adsorption-active MOFs with highly conductive and magnetic components facilitates sensitive, stable, and selective detection of chloramphenicol directly in real water samples. This methodology provides a practical pathway for environmental monitoring and supports the enhancement of water quality management strategies.

1 Introduction

Antibiotics have significantly transformed the management of infectious diseases in humans and animals. Chloramphenicol (CAP), a broad-spectrum phenolic antibiotic, is a notable example. However, due to its associated health risks, particularly its toxic residues in food, CAP has been banned from being used in food-producing animals by the European Union, the United States, and numerous other countries.[1] The accumulation of CAP in the human body can lead to severe conditions, including gray baby syndrome, aplastic anemia, and bone marrow suppression. In addition, CAP has been detected in various water sources worldwide, with concentrations ranging from nanograms per litre (ng L^{-1}) to micrograms per litre (μg L^{-1}).[2] Moreover, residual antibiotics like CAP in aquatic ecosystems contribute to the proliferation of antibiotic-resistant bacteria, which carry antibiotic-resistant genes that are now recognized as emerging contaminants. These genes in drinking water threaten public health and could potentially exacerbate the global antibiotic resistance crisis.[3]

Mitigating these issues requires the detection of this hazardous contaminant in food and environmental samples, which demands cost-effective, robust, and sensitive techniques. Currently, CAP is analyzed using methods such as liquid

[a]Instituto Politécnico Nacional, CICATA Unidad Legaria, LNAgua, CDMX, Mexico

[b]Institute of Chemistry, Faculty of Natural Sciences II, Martin-Luther-Universität Halle-Wittenberg Halle/Saale, Germany

[c]School of Engineering Practice and Technology, McMaster University, 1280 Main Street West Hamilton, Ontario L8S 4L8, Canada. E-mail: ssriniv@mcmaster.ca; rajaba@mcmaster.ca; zleyva@ipn.mx

[d]Department of Civil and Environmental Engineering, Technion − Israel Institute of Technology, Haifa 32000, Israel

chromatography-mass spectrometry (LC-MS),[4] high-performance liquid chromatography (HPLC),[5] capillary electrophoresis (CE),[6] gas chromatography-mass spectrometry (GC-MS),[7] and enzyme-linked immunosorbent assay (ELISA).[8] While these methods effectively detect CPA, they have significant disadvantages, including high costs, labour-intensive procedures, and the need for antibody labelling with enzymatic materials, limiting their suitability for routine analysis.

To overcome the limitations of conventional detection methods, alternative approaches, such as electrochemical sensors using metal–organic framework (MOF) composites, have gained significant attention.[9] Metal–organic frameworks (MOFs) provide key advantages, including exceptional porosity, extensive surface area, customizable pore structures, and well-defined crystalline architectures. These features facilitate efficient analyte concentration and mass transfer, amplifying the electric signal response and enhancing detection sensitivity.[10] In addition to MOFs and MXene materials, a two-dimensional material composed of transition metals and carbon–nitrogen structures holds excellent potential for various electrochemical applications. Its exceptional electrical conductivity, robust mechanical properties, and large surface area have made it useful in several fields, including batteries, supercapacitors, water splitting, and chemical sensors.[11] Magnetite (Fe_3O_4), another valuable material, features iron ions in +2 and +3 oxidation states, providing excellent conductive properties for electrochemical applications. Functionalization of Fe_3O_4 can further modify its electrochemical behavior, making it highly suitable for sensor development.[12]

Combining these materials, Fe_3O_4, MXene, and MOFs, into a composite structure can synergistically enhance their individual properties. This composite not only improves the conductivity of MOFs but also prevents MXene restacking by utilizing MOF particles as interlayer spacers.[13] Furthermore, chemical interactions among functional groups, such as –OH and –O in MXene, –COOH from MOF ligands, and –C–O/–C=O in carbon cloth (CC), promote strong bonding through self-assembly or annealing processes.[14] These enhancements collectively improve the composite's performance as a high-sensitivity electrochemical sensor. Developing an electrochemical sensor with a simple electrode architecture and strong antifouling properties is essential for the direct detection of CAP in complex environmental samples, avoiding labor-intensive pretreatment steps. Therefore, sensitive and reliable detection methods are necessary for environmental monitoring, regulatory compliance, and public health protection. The proposed sensor provides a practical and efficient solution to address this need. This study presents an electrochemical sensing platform that modifies an electrochemically activated screen-printed carbon electrode (SPCE) with a Fe_3O_4@-MXene@Fe-BDC composite. The Fe_3O_4@MXene@Fe-BDC/SPCE sensor demonstrates high sensitivity and low detection limits. The sensor effectively detects CAP even in the presence of interfering molecules and within complex water matrices, showcasing its robustness and practical applicability in environmental monitoring.

2 Experimental section

2.1. Chemicals and reagents

Iron chloride hexahydrate ($FeCl_3 \cdot 6H_2O$, ACS reagent $\geq$99%), iron sulfate heptahydrate ($FeSO_4 \cdot 7H_2O$, ACS reagent, $\geq$99.0%), terephthalic acid (H_2BDC, purity ~98%), sodium hydroxide pellets (NaOH, purity $\geq$97.0%), nitric acid (HNO_3 ACS reagent, 70%), phosphate-buffered saline (PBS, tablet, pH 7.2–7.6), potassium hexacyanoferrate(III) ($K_3Fe(CN)_6$) (ACS reagent, $\geq$99.0%) chloramphenicol (CAP, $\geq$98%), ethanol (CH_3CH_2OH, 99.8%), and methanol (CH_3OH, 99.8%) were supplied by Sigma-Aldrich, Germany. $Ti_3C_2T_x$ MXene multilayer was supplied by Nanochemazone, Canada. N,N-Dimethylformamide (DMF, purity 99.8%) was obtained from Samchun Pure Chemicals, Korea. All reagents and solvents were used as received from commercial suppliers without further purification. The screen-printed electrodes (SPEs) used in this study were TE100 models from Zensor R&D, featuring a 3 mm diameter (0.071 cm^3) carbon working electrode, a carbon counter electrode, and a silver reference electrode.

2.2. Synthesis of Fe_3O_4@MXene@Fe-BDC

2.2.1 Synthesis of Fe-BDC. Fe-BDC MOF was synthesized through a solvothermal process. $FeCl_3 \cdot 6H_2O$ (2.70 g) and H_2BDC (1.66 g) were dissolved in 50 mL of DMF by sonication for 15 min. The solution was placed in a 200 mL Teflon-lined stainless-steel autoclave and heated at 150 °C for 12 hours.[15] After natural cooling, the solid product was collected by centrifugation (4000 rpm). The obtained powder was washed three times with deionized water before being dried in a vacuum at 60 °C for 24 hours.

2.2.2 Synthesis of Fe_3O_4. Fe_3O_4 nanoparticles were prepared using the co-precipitation technique. Initially, 4.53 g of $FeCl_3 \cdot 6H_2O$ was dissolved in 100 mL of acidified water while purging with nitrogen gas for 15 minutes. Subsequently, a solution containing 2.78 g of $FeSO_4 \cdot 7H_2O$ in 100 mL of distilled water was added. Following this, 300 mL of 1.25 mol L^{-1} NaOH solution was introduced gradually under continuous nitrogen flow. The reaction mixture was maintained under constant stirring (100 rpm) and a nitrogen atmosphere at room temperature. After one hour, the resulting black precipitate was collected using a magnet, washed repeatedly with water until neutral pH was achieved, and dried in a vacuum oven at 50 °C for 24 hours.

2.2.3 Synthesis of Fe_3O_4@MXene. 125 mg of Fe_3O_4 and 62.5 mg of MXene were each dispersed separately in 6.25 mL of deionized water using sonication. These two dispersions were then combined and stirred continuously for 3 hours. The resulting composite was collected magnetically, rinsed thrice with deionized water, and dried at 50 °C for 24 hours.

2.2.4 Synthesis of Fe_3O_4@MXene@Fe-BDC. The final composite was synthesized by stirring Fe-BDC (10 mg) and Fe_3O_4@MXene (5 mg) in a ratio of 2 : 1 in a mixture of 3 : 2 deionized water (6 mL) and ethanol (4 mL). After one hour of stirring, the final material was separated using magnetic separation and washed three times with deionized water. The solid product was then dried at 50 °C for 24 h.

© 2026 The Author(s). Published by the Royal Society of Chemistry

Environ. Sci.: Adv., 2026, **5**, 1162–1173 | **1163**

2.3. Analytical instruments

Detailed information on analytical instruments is presented in Section S1.

2.4. Experimental methodology

2.4.1 Electrode cleaning. The pristine screen-printed carbon electrodes (SPCE) were washed using MilliQ water and dried using hot airflow.

2.4.2 Preparation of Fe_3O_4@MXene@Fe-BDC@SPCE zensor electrode. 2.0 mg of Fe_3O_4@MXene@Fe-BDC was added and sonicated in a methanol solution (1.5 mL) to prepare a suspension of the material. After this, the carbon working electrode surface of the washed electrodes was modified with 1 μL of the material and dried using hot airflow (Fig. 1a).

2.4.3 Electrochemical measurements. The electrochemical characterization of the SPCE was conducted using 0.1 M phosphate-buffered saline (PBS) at pH 6, containing 1.0 mM $K_3[Fe(CN)_6]$ and 0.1 M KCl as the redox probe. Two electrochemical techniques were applied: cyclic voltammetry (CV) and electrochemical impedance spectroscopy (EIS). CV measurements were performed over a potential range of −0.5 to +0.9 V with a scan rate of 0.1 mV s^{-1}. EIS data were collected across frequencies from 0.01 mHz to 65 kHz, applying a 5 mV amplitude signal and a scan rate of 100 mV s^{-1}. Additionally, differential pulse voltammetry (DPV) was used to assess the electrochemical response of CAP at varying concentrations in 0.1 M PBS (pH 7.4). The DPV parameters included a potential window from −0.2 to 1.2 V, a step potential of 5 mV, a pulse amplitude of 0.05 V, a pulse width of 0.2 s, and a pulse period of 0.5 s. All measurements were performed at ambient temperature.

2.4.4 Real environmental water sample detection. The river water sample was collected from the Paris River in Ontario, Canada. Without any prior treatment, the sample was spiked with CAP, and its concentration was determined using differential pulse voltammetry (DPV) with the Fe_3O_4@MXene@Fe-BDC-modified SPCE.

3 Results and discussion

3.1. Characterization of Fe_3O_4@MXene@Fe-BDC composite

The diffraction pattern of the synthesized Fe-BDC MOF closely matched the reported patterns of MIL-53(Fe)-DMF (Fe(OH)(BDC, CCDC: 2088536)) and Fe(BDC)(DMF) (CCDC: 2088533).[16] Minor variations in peak positions were observed, which can likely be attributed to the presence coordinated or guest solvent molecules, as previously reported for MIL-53(Fe).[17,18] The Fe_3O_4@MXene composite exhibited characteristic diffraction peaks corresponding to Fe_3O_4 at $2\theta = 29.3°$, 35.2°, and 41.7°, indexed to the (220), (311), and (400) planes (JCPDS Card No. 03-0863),[19] along with peaks of $Ti_3C_2T_x$ MXene at 21.2°, 32.3°, and 41.4° assigned to the (004), (006), and (105) reflections (JCPDS Card No. 032-1383).[20,21] In the PXRD pattern of the Fe_3O_4@MXene@Fe-BDC composite, the characteristic reflections of Fe-BDC remained clearly visible, indicating that the crystalline framework of the MOF was preserved during composite fabrication. The diffraction peaks corresponding to Fe_3O_4@MXene were also retained, although with reduced intensity (Fig. 1a), suggesting successful integration of the components without structural degradation.

The FT-IR spectrum of Fe-BDC revealed bands at 1669 cm^{-1} and 1561 cm^{-1} corresponding to carbonyl stretching and carboxyl groups coordinated with Fe(III) nodes, and a band at
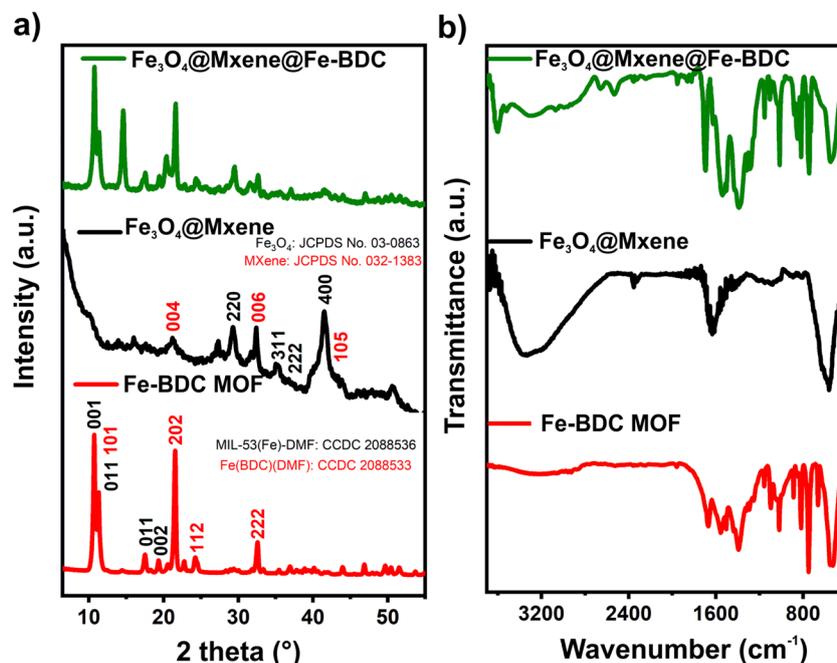

Fig. 1 (a) PXRD pattern; (b) FT–IR spectra of Fe–BDC, Fe_3O_4@MXene, and Fe_3O_4@MXene@ Fe–BDC materials.

539 cm^{-1} attributed to Fe–O bond vibrations, confirming the Fe(III)–COOH coordination.[22] For Fe$_3$O$_4$@MXene, bands at 3357 cm^{-1} (–OH) and 1626 cm^{-1} (C=O) were characteristic of MXene formed after etching, while the high-intensity band at 560 cm^{-1} corresponded to Fe–O stretching in Fe$_3$O$_4$.[23] In the FT-IR spectrum of Fe$_3$O$_4$@MXene@Fe-BDC, the consistent presence of bands from both Fe-BDC and Fe$_3$O$_4$@MXene confirmed successful formation of the final composite (Fig. 1b).

3.2. Characterization of Fe$_3$O$_4$@MXene@Fe-BDC electrode

FT-IR spectroscopy confirmed the successful modification of the carbon working electrode surface of the SPCE with the Fe$_3$O$_4$@MXene@Fe-BDC composite. Upon modification, distinct bands corresponding to the composite's components were observed (Fig. 2b). SEM micrographs further verified the

deposition of the Fe$_3$O$_4$@MXene@Fe-BDC composite on the bare electrode surface (Fig. 2c). Additionally, 2D elemental mapping of the Fe$_3$O$_4$@MXene@Fe-BDC/SPCE revealed an uneven distribution of constituent elements within the composite, attributed to the physical mixing of Fe$_3$O$_4$@MXene and Fe-BDC MOF (Fig. S2).

The X-ray photoelectron spectroscopy (XPS) analysis demonstrated the successful modification of the SPCE working electrode surface with the Fe$_3$O$_4$@MXene@Fe-BDC composite. According to Table S1, which summarizes the atomic percentages of the most concentrated elements in the materials part of the final composite and the surface of the working electrode of the pristine and modified SPCE, a significant enhancement in oxygen levels was observed after electrode modification, which is consistent with the addition of oxygen groups sourced from
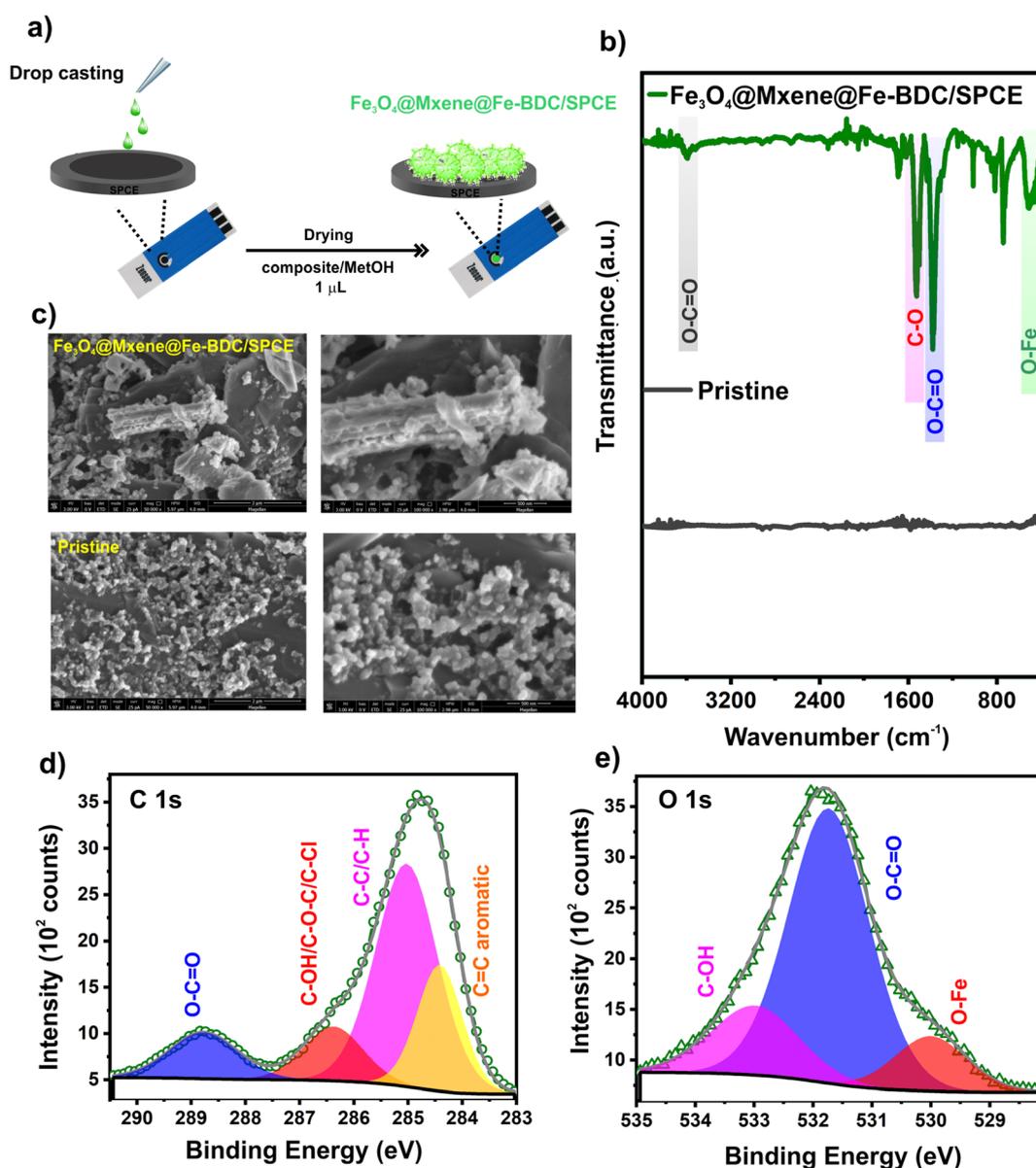

Fig. 2 (a) Graphical depiction of the working electrode surface modification with Fe$_3$O$_4$@MXene@Fe-BDC; (b) FT-IR spectra, (c) SEM micrographs of pristine (SPCE), Fe$_3$O$_4$@MXene@Fe-BDC/SPCE, (d) C 1s, and (e) O 1s high-resolution signal spectra of Fe$_3$O$_4$@MXene@Fe-BDC/SPCE.

the MOF and oxide components. Additionally, Ti signals confirm the successful incorporation of MXene into the composite. All expected elements from Fe_3O_4, MXene, and Fe-BDC MOF were evidenced in the modified electrode, supporting the effective assembly of the hybrid material on the working electrode surface of the SPCE. All spectra were calibrated for charging effects using the C1s peak of organic carbon as a reference (C–C/C–H) to 285.0 eV. The high-resolution C 1s spectrum revealed four main components (Fig. 2d): C=C aromatic at 284.4 eV, C–C/C–H at 285.0 eV, COH/C–O–C/C–Cl at 286.4 eV, and O–C=O at 288.8 eV. These components are characteristic of Fe-BDC MOF and functional groups on the MXene and Fe_3O_4 surfaces. Also, in the O 1s region (Fig. 2e), three distinct peaks were assigned to O–Fe at 530.0 eV, O=C–O at 531.7 eV, and C–OH at 533.0 eV, further evidencing the coexistence of metal–oxygen bonding and oxygenated surface functionalities.[24,25]

3.3. Electrochemical characterization

3.2.1 Electrochemical performance of the modified electrodes. MOF-modified electrodes represent a significant advancement in the electrochemical detection of CAP, delivering remarkable sensitivity, selectivity, and stability. These properties render them well-suited for real-world environmental monitoring. Ongoing material optimization is expected to develop even more efficient sensing platforms that comply with strict regulatory standards for antibiotic residues.[26] Incorporating MOFs onto SPCEs generally boosts the availability of electroactive sites, thereby enhancing sensitivity and selectivity toward specific analytes.[27] Furthermore, the porous structure of MOFs promotes efficient ion transport and electron transfer kinetics, which are critical for real-world sensing applications. The highly effective surface area maintained by MOF-based sensors ensures stability and reproducibility of responses over time, an essential factor for reliable practical usage.[28]

Determining the surface area of Fe_3O_4@MXene@Fe-BDC/SPCE is essential for evaluating their electrochemical performance in sensing applications. The surface area directly impacts the availability of active sites for electrochemical reactions, significantly influencing sensitivity and detection limits.[29] Cyclic voltammetry is commonly used to assess the electroactive surface area of modified electrodes. The current response from a redox probe $K_3[Fe(CN)_6]$ can be analyzed to calculate the surface area using the Randles–Sevcik equation:

$$I_p = 2.69 \times 10^5 n^{3/2} A D^{1/2} C v^{1/2} \tag{1}$$

Where I_p is the peak current, n is the number of electrons transferred, A is the electrode area, D is the diffusion coefficient, C is the concentration of the redox species, and v is the scan rate. By rearranging this equation, the effective surface area (A) can be calculated based on experimental data.[30]

Fig. 3a and c displays the cyclic voltammetry (CV) profiles of the bare SPCE and the Fe_3O_4@MXene@Fe-BDC/SPCE electrodes recorded in 1.0 mM aqueous solution of $K_3[Fe(CN)_6]$ and 0.1 M KCl, with scan rates varying from 10 to 100 mV s^{-1}. The

unmodified SPCE showed peak-to-peak separation (ΔE_p) redox peaks of 0.17 V. In contrast, the Fe_3O_4@MXene@Fe-BDC/SPCE electrode demonstrated increased peak current (I_p) and a reduced ΔE_p of 0.12 V, indicating enhanced electron transfer kinetics. The Fe_3O_4@MXene@Fe-BDC/SPCE electrode achieved the highest redox peak currents, attributed to the superior electrical conductivity and larger surface area provided by the synergistic combination of Fe_3O_4@MXene@Fe-BDC composite.[31] Furthermore, Fig. 3b and d illustrates the linear relationship between the square root of the scan rate and the peak current, described by the equation I_p (μA) = 1.84 + 69.53 $v^{1/2}$ (mV s^{-1}) (R^2 = 0.99), enabling the calculation of the effective surface area using the slope of the I_p–$v^{1/2}$ curve in eqn (1). The effective surface area of the Fe_3O_4@MXene@Fe-BDC/SPCE electrode was determined to be 0.095 cm^2, significantly larger than the 0.049 cm^2 of the bare SPCE electrode. This increase in surface area, facilitated by the Fe_3O_4@MXene@Fe-BDC/SPCE modification, is critical for improving the electrode's electrochemical sensing performance in detecting CAP.

3.2.2 Electrochemical impedance spectroscopy (EIS). Electrochemical Impedance Spectroscopy (EIS) evaluates the impedance behavior of an electrochemical system over a spectrum of frequencies, providing a detailed characterization of processes occurring at the electrode surface. This technique is invaluable for understanding charge transfer resistance (R_{ct}) and overall interfacial kinetics, which are critical for optimizing sensor performance. In the impedance spectra, the semicircle appearing at higher frequencies is associated with electron transfer limitations, whereas the linear part at lower frequencies reflects diffusion-controlled behavior.[32,33] Additionally, EIS can provide insights into the electrode's effective surface area by analyzing R_{ct} and double-layer capacitance; changes in these parameters indicate surface modifications. In addition, with the R_{ct} values, it is possible to evaluate the effectiveness of electrode modifications in enhancing sensor performance.[32] The impedance data were analyzed using an equivalent electrical circuit incorporating a Warburg diffusion element (Fig. 4), which is well suited to systems in which mass transport and adsorption occur through surface channels or microstructural defects.[34] In this model, the charge-transfer resistance (R_{ct}) is arranged in series with the Warburg impedance (W), and this series combination is connected in parallel with a constant phase element (C) to account for non-ideal capacitive behavior at the electrode interface. The circuit is completed by including the solution resistance (R_s) in series, allowing clear differentiation and quantification of the bulk electrolyte resistance, interfacial electron-transfer processes, and diffusion-controlled ion transport.

This study evidenced a small semicircle region in the modified SPCE electrode (Fig. 4b), suggesting a significantly reduced electron-transfer resistance.[35] Also, the R_{ct} value for the bare SPCE electrode was measured at 3.89 kΩ, while the modified Fe_3O_4@MXene@Fe-BDC/SPCE electrode significantly reduced R_{ct} to 1.89 kΩ. This reduction in R_{ct} demonstrates the enhanced electron transfer kinetics achieved by integrating Fe_3O_4@MXene@Fe-BDC/SPCE, directly contributing to improved sensor performance. These findings underscore the significance of EIS in developing advanced electrochemical
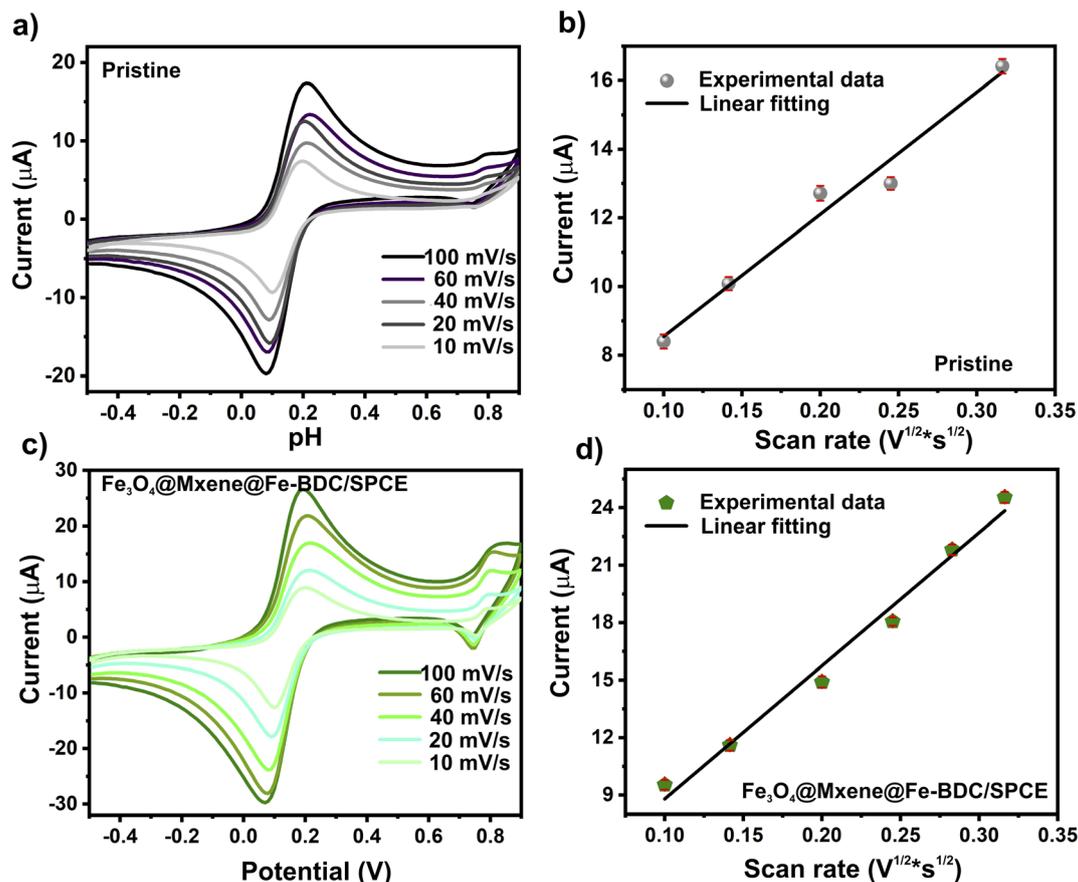
1166 | Environ. Sci.: Adv., 2026, **5**, 1162–1173

© 2026 The Author(s). Published by the Royal Society of Chemistry

Fig. 3   CV of 1.0 mM $K_3[Fe(CN)_6]$ containing 0.1 M KCl solution for (a) pristine electrode; (c) Fe_3O_4@MXene@Fe-BDC/SPCE and corresponding linear plot for current against the square root of scan rate for (b) pristine electrode; (d) Fe_3O_4@MXene@Fe-BDC/SPCE.
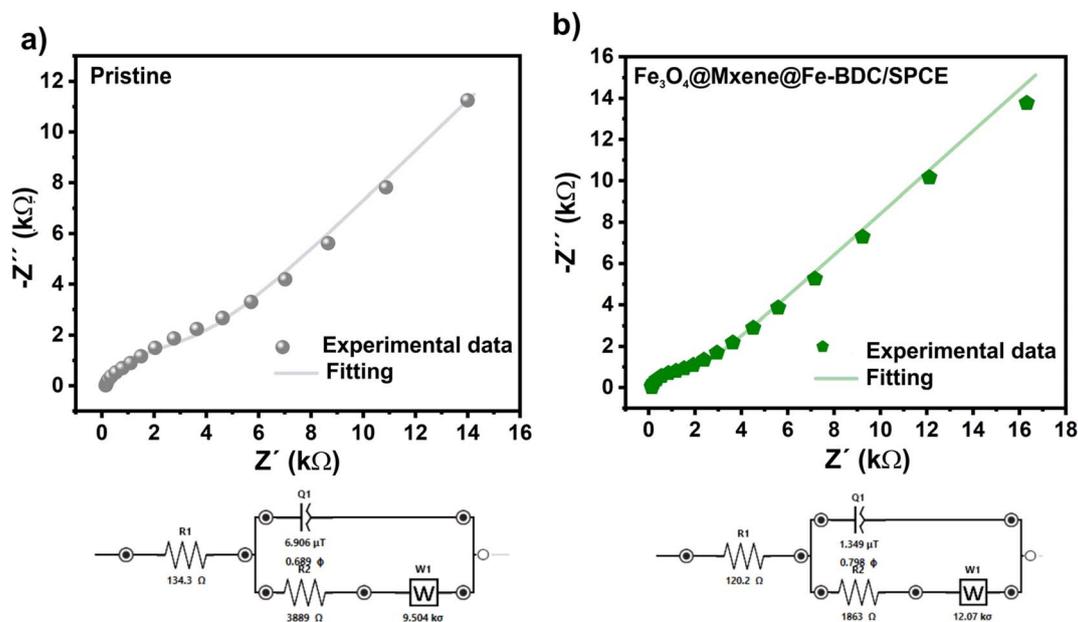

Fig. 4   EIS plots of 1.0 mM $K_3[Fe(CN)_6]$ containing 0.1 M KCl solution for (a) pristine electrode, (b) Fe_3O_4@MXene@Fe-BDC/SPCE, and equivalent circuit for EIS tests.

sensors with enhanced functionality. The increased electro-active surface area and reduced electron-transfer resistance indicate that Fe$_3$O$_4$@MXene@Fe-BDC is a promising candidate for developing electrochemical sensors.

3.3. Optimization of CPA detection conditions

Key parameters such as the amount of Fe$_3$O$_4$@MXene@Fe-BDC deposited on the electrode, the pH, and the scan rate were systematically optimized to develop an efficient sensor. These factors were evaluated using the Differential Pulse Voltammetry (DPV) to ensure optimal sensor performance.

3.3.1 Influence of Fe$_3$O$_4$@MXene@Fe-BDC amount. The effect of Fe$_3$O$_4$@MXene@Fe-BDC amount on the sensor's performance is shown in Fig. 5a. The current response to CAP decreased as the amount of material used to modify the working electrode surface increased. This reduction in current signals is attributed to the reduced surface area of the Fe$_3$O$_4$@-MXene@Fe-BDC/SPCE sensor, which lowered the adsorption of CAP molecules onto the electrode surface. Therefore, 1 μL was selected as the optimal volume of the final composite solution for the best performance.[36]

3.3.2 Influence of pH. The pH of the electrolyte solution plays a crucial role in the electrochemical detection of CAP. It significantly affects the CAP's ionization state, solubility, and interaction with the electrode surface, influencing the sensor's sensitivity and selectivity. CAP is a weak acid with a pK_a of around 9.1. In acidic conditions (low pH), CAP mainly exists in its protonated form, while in alkaline conditions (high pH), it becomes deprotonated. This change in ionization affects how CAP interacts with the final composite-modified electrode surface and alters its electrochemical behavior.[37] Fig. 5c illustrates that the current response of CAP initially enhanced with rising pH. However, beyond a certain point, the current decreased as the pH increased.[38] This decrease may be related to CAP's protonation in strongly acidic buffer solutions. At the same time, in neutral or basic environments, the deprotonation of CAP can hinder electron transfer during the detection process.[39] Based on these observations, a pH of 6.0 was selected as the optimal condition for CAP detection.

3.3.3 Influence of scan rate. The impact of the scan rate on the CPA detection process is shown in Fig. 5b. The current response of the CAP changed when the scan rate was varied from 10 to 100 mV s^{-1}. The peak current (I_p) was plotted against the square root of the scan rate ($v^{1/2}$), with a linear relationship, described by the equation I_p (μA) = -17.76–61.98 $v^{1/2}$ (V s^{-1}), with a correlation coefficient (R^2) of 0.98 (Fig. 5d). This shows that the electrode reaction is surface-controlled, consistent with previous studies.[40] Among the evaluated conditions, 100 mV s^{-1}
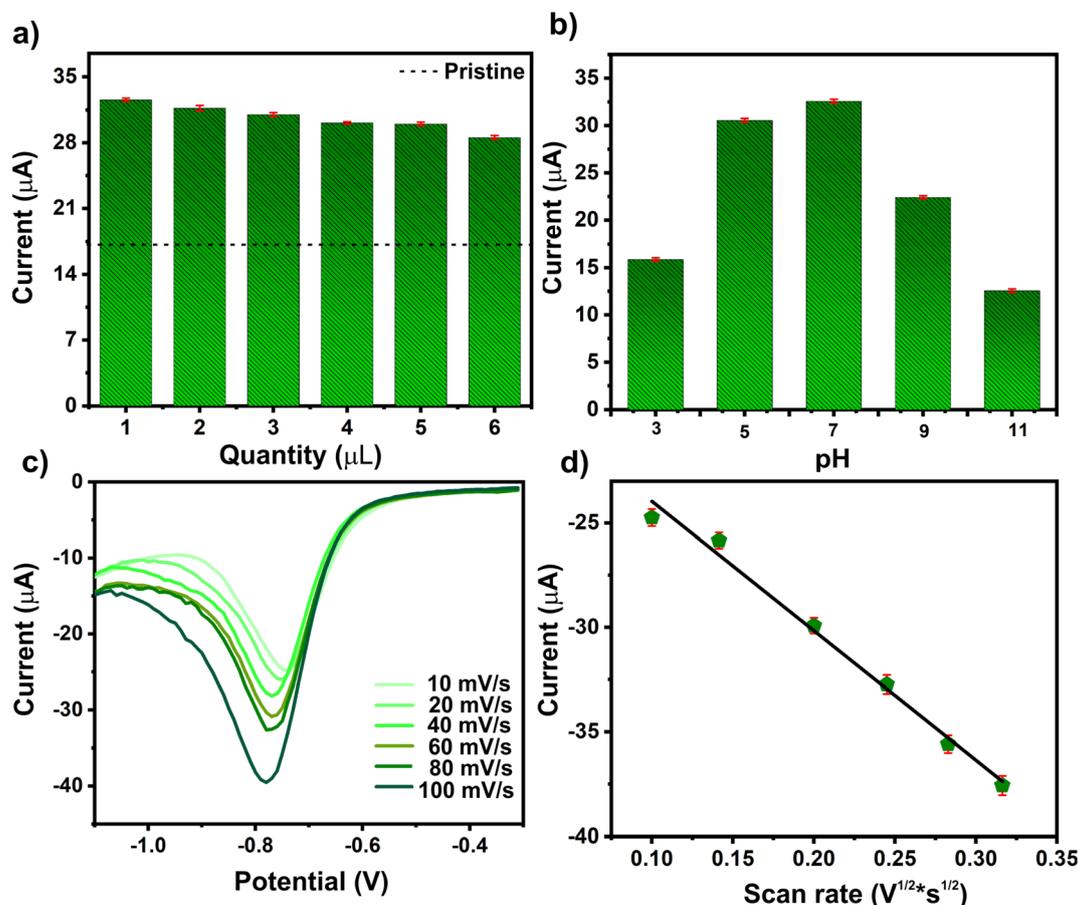

Fig. 5 Effect of different parameters on the peak current. (a) Amount of Fe$_3$O$_4$@MXene@Fe-BDC/SPCE in μL, (b) the scan rate, and (c) pH value, and (d) linear plot for current against the square root of scan rate. Conditions: [CAP] = 50 ppm in PBS.
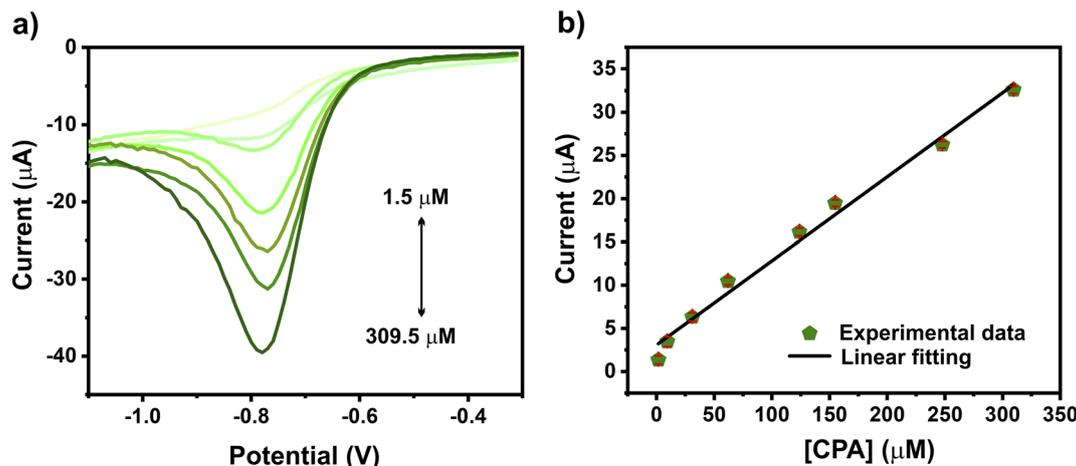
Fig. 6 (a) Representative differential pulse voltammetry response of CAP at Fe_3O_4@MXene@Fe-BDC/SPCE sensor with different CAP concentrations; (b) the relation between the peak current and the concentration of CAP.

provided a higher and well-defined current response with good peak shape and signal stability, while maintaining a clear diffusion-controlled behavior. Therefore, 100 mV s^{-1} was selected as the optimal scan rate to ensure enhanced signal intensity without compromising the electrochemical mechanism or peak resolution.

3.4. Quantitative analysis of CAP

Fig. 6a depicts CAP's differential pulse voltammetry response at varying CAP concentrations using the Fe_3O_4@MXene@Fe-BDC/SPCE sensor. The relationship between peak current and CAP concentration is often linear over specific ranges, allowing for straightforward quantification.[41] A progressive enhancement in peak current was detected as CAP concentrations varied from 1.5 to 309.5 μM. Fig. 6b presents a linear correlation between CAP concentration and peak current, described by the equation I_p (μA) = 0.09 [CAP] (μM) + 3.09 (R^2 = 0.99).

The sensitivity of the Fe_3O_4@MXene@Fe-BDC/SPCE was calculated using eqn (2):

$$\text{Sensitivity} = \frac{S}{A} \qquad (2)$$

where S is the slope of the calibration plot (μA μM^{-1}), and A is the active surface area of the electrode (cm^2).[42] The sensitivity of the Fe_3O_4@MXene@Fe-BDC/SPCE sensor was 0.95 μA μM^{-1} cm^{-2}. The enhanced sensitivity of the SPCE following modification with Fe_3O_4@MXene@Fe-BDC/SPCE can be attributed to improved electrical conductivity, increased adsorption capacity, and a larger electroactive surface area. These enhancements are consistent with the findings from EIS analyses.

The limit of detection (LOD) of the modified electrode was calculated using eqn (3):

$$\text{LOD} = \frac{3\sigma}{S} \qquad (3)$$

Based on the IUPAC definition, where σ represents the standard deviation of three blank measurements and S denotes the slope of the calibration curve.[43] The proposed method shows a LOD of 0.26 μM. The analytical performance of Fe_3O_4@MXene@Fe-BDC/SPCE was compared with previously reported electrodes (Table 1), highlighting that the Fe_3O_4@MXene@Fe-BDC/SPCE sensor has better sensitivity and LOD than previously reported sensors.

Table 1 Electrochemical sensors reported for CAP detection[a]

Modified electrodes	Determination method	LOD (μM)	Linear range (μM)	Sensitivity (μA μM^{-1} cm^{-2})	Reference
AuNPs/N-G/GCE	LSV	0.59	2–80.0	—	44
CuCo$_2$O$_4$/CuFe$_2$O$_4$/GCE	DPV	0.66	2.5–50	—	45
AuNPs/GO/GCE	Amperometry	0.25	1.50–2.95	3.810	38
Au/SPPtEs	DPV	0.60	0.25–50	0.0318 (cm^2)	46
Fe-Silk PNC/PGE	DPV	0.57	1.00–200.00	—	47
MoS2-rGO/GCE	DPV	1.00	5.0–35.0	3.581	48
Cu–MoS$_2$/SPCE	DPV	0.45	1.0–50.0	0.141 (μA μM^{-1})	49
Z-800/RGO/GCE	DPV	0.25	1.0–180.0	—	50
rGO/Co$_3$O$_4$/GCE	CV	0.55	1–2000	—	51
Sn/rGO/SPCE	DPV	0.20	0.5–30.0 and 30.0–100.0	0.934 and 0.278	52
Fe_3O_4@MXene@Fe-BDC/SPCE	DPV	0.26	1–309	0.95	This work

^{a} LSV: Linear Sweep Voltammetry.

© 2026 The Author(s). Published by the Royal Society of Chemistry

Environ. Sci.: Adv., 2026, **5**, 1162–1173 | **1169**

3.5. Mechanism of sensing: CAP behavior on the Fe₃O₄@MXene@Fe-BDC/SPCE

The proposed adsorption and redox interaction mechanism is based on well-established electrochemical pathways of chloramphenicol reported in previous studies, which describe the $4e^-/4H^+$ reduction of the nitro group ($-NO_2$) to the hydroxylamine derivative and its reversible conversion to the nitroso intermediate (Fig. 7a). This cyclic transformation results in a distinct cathodic reduction peak, highlighting the efficient redox response of the modified electrode.[53,54] In this work, the mechanistic interpretation is supported by precedent in the literature and spectroscopic evidence from XPS. Here, the surface chemistry of the composite material plays a vital role in the adsorption process. Functional groups rich in oxygen, such as carboxyl ($-COOH$), phenol ($-OH$), and ether ($C-O-C$), facilitate the formation of hydrogen bonds with the hydroxyl groups present in CAP. Regardless of pH, these interactions are supported by the robust nature of hydrogen bonds, alongside other forces like electrostatic attraction, π–π stacking between the electrode's π-electron system and CAP's aromatic rings, and Fe–O bridge formation (Fig. 7b).

XPS analysis further supports these mechanisms. For instance, after CAP interaction, noticeable changes are observed in the C 1s spectrum at 284.3 eV (C=C aromatic), 285.0 eV (C–C/

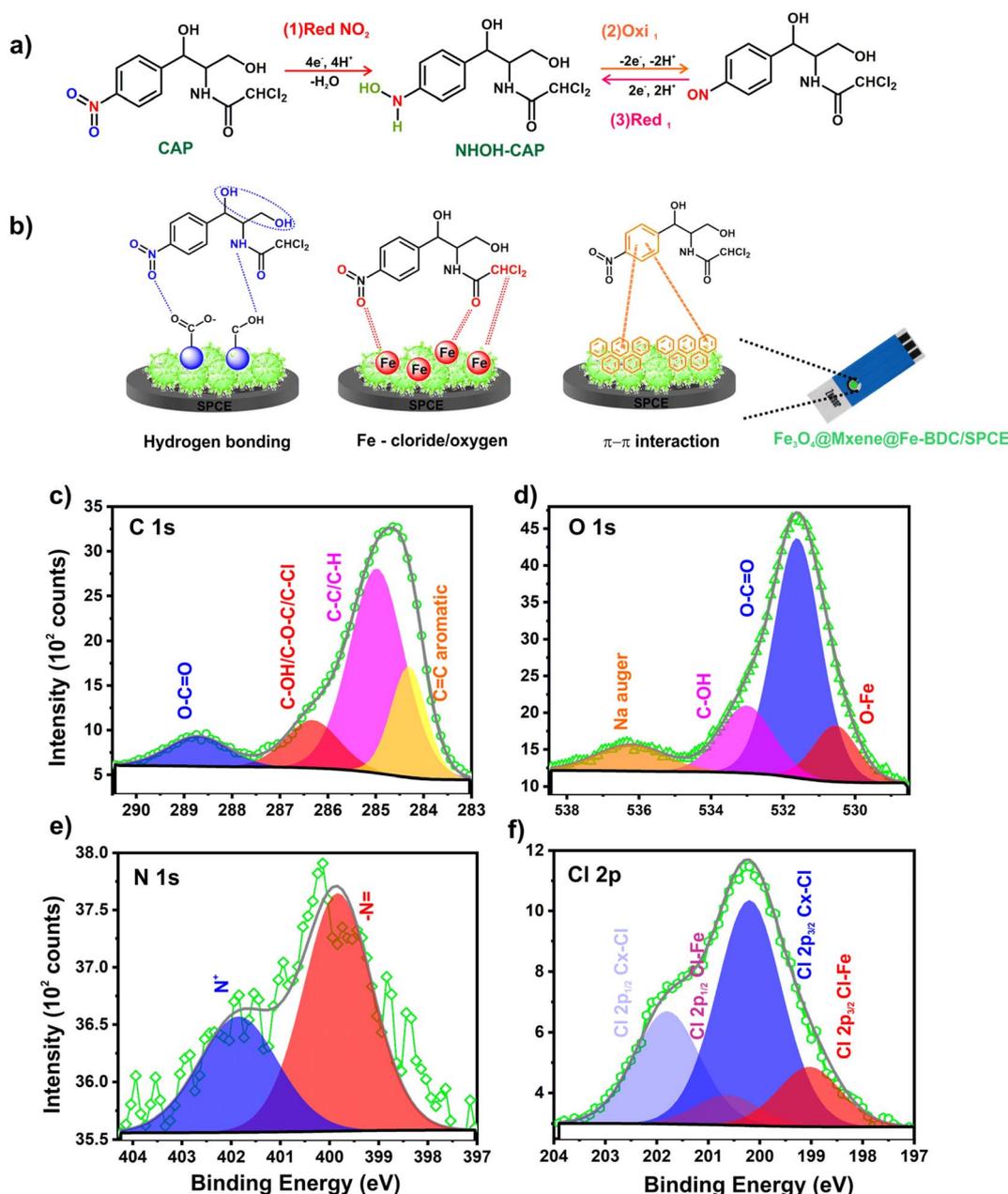**Fig. 7** (a) Redox reaction mechanism of CAP, (b) proposed mechanism of CAP over Fe₃O₄@MXene@Fe-BDC/SPCE, and (c) C 1s, (d) O 1s, (e) N 1s, and (f) Cl 2p high-resolution signal spectra of Fe₃O₄@MXene@Fe-BDC/SPCE after CAP sensing.

C–H), 286.3 eV (COH/C–O–C/C–Cl), and 288.7 eV (O–C═O), indicating variations in surface carbon environments due to π–π interactions and hydrogen bonding. In the O 1s region, the components at 530.5 eV (O–Fe), 531.6 eV (O═C–O), and 533.0 eV (C–OH), as well as the appearance of a peak at 536.2 eV (Na Auger), suggest strong involvement of oxygenated sites in the binding process, primarily through H-bonding and Fe–O coordination. Additionally, new signals in the N 1s region at 399.8 eV (–N═) and 401.8 eV (N$^+$), and in the Cl 2p spectrum at 199.0 eV (Cl–Fe) and 200.2 eV (C–Cl),[24] further support the incorporation and interaction of CAP with the electrode surface.[55] The emergence and shifting of these signals confirm that the adsorption mechanism involves a combination of π–π stacking, hydrogen bonding, electrostatic forces, and metal–oxygen (Fe–O) bridging interactions. These complementary interactions collectively enhance CAP adsorption and facilitate its redox transformation on the Fe$_3$O$_4$@MXene@Fe-BDC/SPCE surface.[56]

3.6. Repeatability and stability of Fe$_3$O$_4$@MXene@Fe-BDC/SPCE

Multiple tests were carried out to evaluate the consistency and long-term stability of the Fe$_3$O$_4$@MXene@Fe-BDC/SPCE sensor. Six identical electrodes were fabricated to detect CAP, with a material amount of 1 μM over each electrode. Ten consecutive measurements were performed on the same Fe$_3$O$_4$@MXene@Fe-BDC/SPCE sensor for repeatability testing in the presence of 50 ppm CAP (Fig. 8a). The current responses' relative standard deviation (RSD) of 1.23% demonstrates the modified electrode's excellent repeatability.[57]

The sensor's long-term stability was also examined by measuring its current response to 50 μM CAP over five days. A peak current retention of 95.7% was observed after 20 days of storage at ambient temperature (Fig. 8b), demonstrating the remarkable stability of the Fe$_3$O$_4$@MXene@Fe-BDC/SPCE
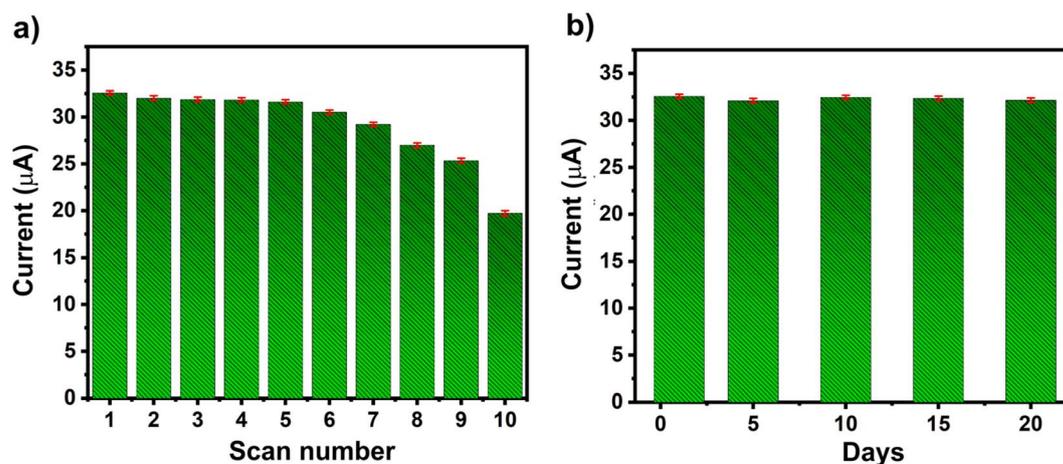

Fig. 8 (a) Reproducibility of the Fe$_3$O$_4$@MXene@Fe-BDC/SPCE sensor for [CAP] = 50 ppm in PBS; (b) stability of the sensor for [CAP] = 50 ppm in PBS in 20 days.
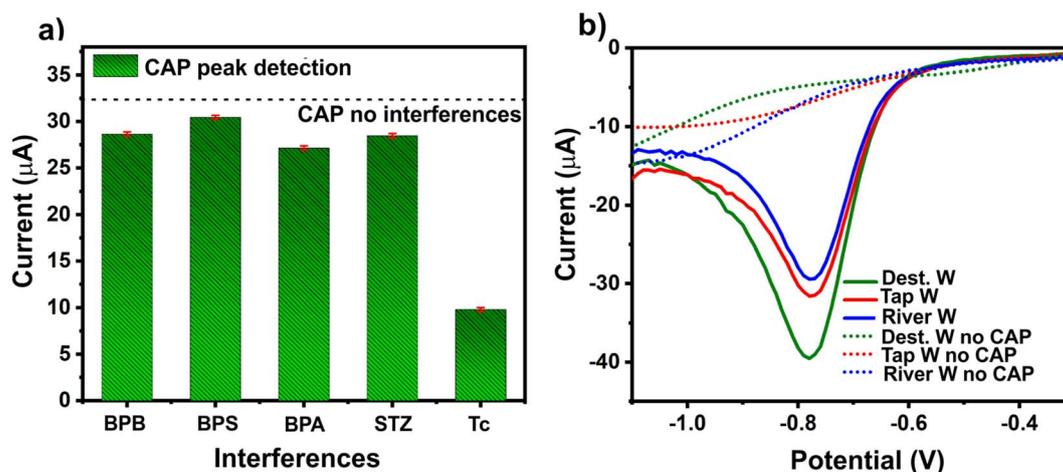

Fig. 9 (a) Selectivity of the Fe$_3$O$_4$@MXene@Fe-BDC/SPCE sensor towards the response of CAP in the presence of other pollutants for [CAP, pollutants] = 50 ppm; (b) differential pulse voltammetry response measurements with Fe$_3$O$_4$@MXene@Fe-BDC/SPCE sensor in distilled water (Dest. W), tap water (Tap W), and river water (River W).

© 2026 The Authors. Published by the Royal Society of Chemistry

Environ. Sci.: Adv., 2026, **5**, 1162–1173 | 1171

sensor. These results highlight the sensor's reliability for practical applications.[58]

3.7. Interference and determination of CAP in real water

Selectivity and interference are critical parameters for assessing the efficiency of electrochemical sensors. In this study, the selectivity of the Fe$_3$O$_4$@MXene@Fe-BDC/SPCE sensor was evaluated in the presence of waterborne common pollutants, including bisphenol B (BPB), bisphenol A (BPA), bisphenol S (BPS), and sulfamethazine (STZ). The current response values demonstrated that the sensor selectively detected CAP over these competing pollutants. This selectivity is attributed to the favorable selectivity coefficients of CAP against other molecules, outstanding selectivity, and resistance to interference, establishing a strong foundation for its use in practical detection scenarios.[59]

The Fe$_3$O$_4$@MXene@Fe-BDC/SPCE sensor was utilized to detect CAP in real water samples using the standard addition method to assess its practical feasibility. The water sample was taken from the Paris River, Ontario, Canada, for the real water experiments. Additionally, tap water (Tap W) and river water (River W) samples were spiked with 50 ppm CAP, and the final CAP concentrations were analyzed using differential pulse voltammetry. Each sample was analyzed in triplicate. As shown in Fig. 9b, the sensor exhibited reliable performance in complex water matrices, comparable to its performance in distilled water (Dest. W). These outcomes support the robustness and effectiveness of the method for practical CAP detection applications.[60]

4 Conclusion

A new electrochemical sensor was developed in this study, featuring a screen-printed carbon electrode (SPCE) modified with Fe$_3$O$_4$@MXene@Fe-BDC for chloramphenicol (CAP) detection in complex water environments. The synergistic integration of Fe$_3$O$_4$, MXene, and Fe-BDC MOF resulted in a composite with significantly improved electrochemical features, including better conductivity, increased surface activity, and higher adsorption efficiency. The sensor demonstrated excellent analytical performance, achieving a low detection limit of 0.26 μM and a high sensitivity of 0.95 μA μM^{-1} cm^{-2}. Additionally, modification of the electrode resulted in a marked decrease in charge transfer resistance, as evidenced by EIS measurements, validating the enhanced conductivity of the sensor surface. The presence of carboxyl, phenolic, and Fe–O groups in the composite, confirmed by XPS analysis, was key to enhancing adsorption and electron transfer through hydrogen bonds, π–π stacking, and metal–oxygen bridges. Furthermore, the sensor demonstrated high selectivity against common interfering pollutants and excellent stability, retaining over 95% of its initial signal after 20 days. Its effective performance in real water samples, including river and tap water, confirms its potential for practical environmental applications. The developed platform offers a useful and reliable approach for rapidly detecting CAP in environmental applications.

Conflicts of interest

There are no conflicts to declare.

Data availability

The data supporting this article have been included as part of the supplementary information (SI). Supplementary information: TEM images of the samples (Fig. S1); EDS mapping of the samples (Fig. S2); XPS peak-fitting results for the element high-resolution signals from the samples (Tables S1–S5). See DOI: https://doi.org/10.1039/d5va00474h.

Acknowledgements

References

1 N. T. Anh, N. X. Dinh, T. N. Pham, L. K. Vinh, L. M. Tung and A. T. Le, *RSC Adv.*, 2021, **11**, 30544–30559.

2 C. Li, F. Luo, H. Duan, F. Dong, X. Chen, M. Feng, Z. Zhang, L. Cizmas and V. K. Sharma, *Sep. Purif. Technol.*, 2019, **211**, 564–570.

3 J. Lin, K. Zhang, L. Jiang, J. Hou, X. Yu, M. Feng and C. Ye, *Sci. Total Environ.*, 2022, **850**, 158059.

4 M. Ramos, P. Muñoz, A. Aranda, I. Rodriguez, R. Diaz and J. Blanca, *J. Chromatogr. B*, 2003, **791**, 31–38.

5 H. Chen, H. Chen, J. Ying, J. Huang and L. Liao, *Anal. Chim. Acta*, 2009, **632**, 80–85.

6 W. Jin, X. Ye, D. Yu and Q. Dong, *J. Chromatogr. B Biomed. Sci. Appl.*, 2000, **741**, 155–162.

7 A. Gantverg, I. Shishani and M. Hoffman, *Anal. Chim. Acta*, 2003, **483**, 125–135.

8 J. O. Wesongah, G. A. Murilla, A. N. Guantai, C. Elliot, T. Fodey, A. Cannavan and J. Vet, *Pharmacol. Ther.*, 2007, **30**, 68–73.

9 N. Kajal, V. Singh, R. Gupta and S. Gautam, *Environ. Res.*, 2022, **204**, 112320.

10 W. Zhang, X. Li, X. Ding, K. Hua, A. Sun, X. Hu, Z. Nie, Y. Zhang, J. Wang, R. Li and S. Liu, *RSC Adv.*, 2023, **13**, 10800–10817.

11 J. Wang, Q. Xu, Y. Yang, J. Liu, W. Kong and L. Shi, *Talanta*, 2024, **268**, 125344.

12 F. Mollarasouli, E. Zor, G. Ozcelikay and S. A. Ozkan, *Talanta*, 2021, **226**, 122108.

13 G. Manasa and C. S. Rout, *Mater. Adv.*, 2024, **5**, 83–122.

14 Z. H. Lu, Q. Tian, D. D. Zhou, M. Chen, Y. W. Cao, L. Y. Zhuang, X. Liu, Z. H. Yang and I. A. Senosy, *J. Environ. Chem. Eng.*, 2022, **10**, 108037.

15 H. R. Mahdipoor, R. Halladj, E. Ganji Babakhani, S. Amjad-Iranagh and J. Sadeghzadeh Ahari, *RSC Adv.*, 2021, **11**, 5192–5203.

16 D. Bara, E. G. Meekel, I. Pakamore, C. Wilson, S. Ling and R. S. Forgan, *Mater. Horiz.*, 2021, **8**, 3377–3386.

17 C. Ajpi, N. Leiva, A. Lundblad, G. Lindbergh and S. Cabrera, *J. Mol. Struct.*, 2023, **1272**, 134127.

18 F. Millange, N. Guillou, R. I. Walton, J. M. Grenèche, I. Margiolaki and G. Férey, *Chem. Commun.*, 2008, 4732–4734.

19 I. Bezverkhyy, G. Weber and J. P. Bellat, *Microporous Mesoporous Mater.*, 2016, **219**, 117–124.

20 V. Ankalgi, M. A. Belgami, B. Kulkarni, S. M. Jeong and C. S. Rout, *Sensors & Diagnostics*, DOI: 10.1039/d5sd00187k.

21 R. P. Vadivel, B. Arumugam, R. Surya, K. Venkatesh, C.-L. Chen, S. Sakthinathan, X. Arulanandam, T.-W. Chiu and S. K. Ramaraj, *ACS Appl. Eng. Mater.*, 2025, **3**, 2919–2932.

22 A. Li, X. Yang and J. Chen, *RSC Adv.*, 2021, **11**, 10540–10547.

23 X. Xu, Y. Zhou, S. Li, Y. Lin, S. Zhang and Q. Guan, *J. Environ. Chem. Eng.*, 2022, **10**, 108702.

24 *X-ray Photoelectron Spectroscopy (XPS) Reference Pages: Chlorine*, https://www.xpsfitting.com/2012/04/chlorine.html, accessed 8 May 2025.

25 A. Jeyaseelan, M. Naushad, T. Ahamad and N. Viswanathan, *J. Environ. Chem. Eng.*, 2021, **9**, 104563.

26 J. Zhu, W. Wen, Z. Tian, X. Zhang and S. Wang, *Talanta*, 2023, **260**, 124613.

27 P. Janjani, U. Bhardwaj, M. Agarwal, R. Gupta and H. S. Kushwaha, *Environ. Technol.*, 2024, **45**, 2649–2659.

28 M. Saraban, A. Numnuam, N. Nontipichet, T. Kangkamano, P. Thavarungkul, P. Kanatharana and S. Khumngern, *New J. Chem.*, 2024, **48**, 3638–3645.

29 A. G. M. Ferrari, C. W. Foster, P. J. Kelly, D. A. C. Brownson and C. E. Banks, *Biosensors*, 2018, **8**, 53.

30 C. Celesti, S. V. Giofrè, C. Espro, L. Legnani, G. Neri and D. Iannazzo, *Sensors*, 2024, **24**, 4935.

31 N. Z. M. Azman, P. N. S. Zainal and S. A. A. Ahmad, *PLoS One*, 2020, **15**(6), DOI: 10.1371/JOURNAL.PONE.0234148.

32 S. Jafari, S. M. Pourmortazavi, A. Ehsani and S. Mirsadeghi, *Sci. Rep.*, 2024, **14**, 1–12.

33 X. Zhang, Y. C. Zhang and J. W. Zhang, *Talanta*, 2016, **161**, 567–573.

34 N. Ben Messaoud, A. Ait Lahcen, C. Dridi and A. Amine, *Sens. Actuators B Chem.*, 2018, **276**, 304–312.

35 X. Chen, Y. Wang, J. Zhou, W. Yan, X. Li and J. J. Zhu, *Anal. Chem.*, 2008, **80**, 2133–2140.

36 T. Yang, H. Chen, T. Ge, J. Wang, W. Li and K. Jiao, *Talanta*, 2015, **144**, 1324–1328.

37 S. Suganthi, K. Ahmad and T. H. Oh, *Molecules*, 2024, **29**, 5373.

38 R. Karthik, M. Govindasamy, S. M. Chen, V. Mani, B. S. Lou, R. Devasenathipathy, Y. S. Hou and A. Elangovan, *J. Colloid Interface Sci.*, 2016, **475**, 46–56.

39 T. Alizadeh, M. R. Ganjali, M. Zare and P. Norouzi, *Food Chem.*, 2012, **130**, 1108–1114.

40 W. Zhang, Z. Zhang, Y. Li, J. Chen, X. Li, Y. Zhang and Y. Zhang, *Sens. Actuators B Chem.*, 2017, **247**, 756–764.

41 J. Yin, H. Ouyang, W. Li and Y. Long, *Biosensors*, 2023, **13**, 116.

42 A. Paisanpisuttisin, P. Poonwattanapong, P. Rakthabut, P. Ariyasantichai, C. Prasittichai and W. Siriwatcharapiboon, *RSC Adv.*, 2022, **12**, 29491–29502.

43 E. Demir and H. Silah, *Chemosensors*, 2020, **8**, 25.

44 J. Borowiec, R. Wang, L. Zhu and J. Zhang, *Electrochim. Acta*, 2013, **99**, 138–144.

45 T. N. Pham, N. Van Cuong, N. X. Dinh, H. Van Tuan, V. N. Phan, N. T. Lan, M. H. Nam, T. D. Thanh, V. D. Lam, N. Van Quy, T. Q. Huy, M.-H. Phan and A.-T. Le, *J. Electrochem. Soc.*, 2021, **168**, 026506.

46 N. T. Hue, T. N. Pham, N. X. Dinh, H. Van Tuan, N. T. T. Thuy, M. H. Nam, V. D. Lam, A. T. Le and T. Q. Huy, *J. Electron. Mater.*, 2022, **51**, 1669–1680.

47 W. Chang, Y. Zhu, Y. Ma, Z. Zheng and C. Wang, *Curr. Anal. Chem.*, 2022, **18**, 1017–1028.

48 S. Gao, Y. Zhang, Z. Yang, T. Fei, S. Liu and T. Zhang, *J. Alloys Compd.*, 2021, **872**, 159687.

49 N. T. Anh, N. X. Dinh, T. N. Pham, L. K. Vinh, L. M. Tung and A. T. Le, *RSC Adv.*, 2021, **11**, 30544–30559.

50 Y. Yuan, X. Xu, J. Xia, F. Zhang, Z. Wang and Q. Liu, *Microchim. Acta*, 2019, **186**(3), 191.

51 Q. Yuan, Y. Liu, C. Ye, H. Sun, D. Dai, Q. Wei, G. Lai, T. Wu, A. Yu, L. Fu, K. W. A. Chee and C. Te Lin, *Biosens. Bioelectron.*, 2018, **111**, 117–123.

52 S. Bunnasit, K. Thamsirianunt, R. Rakthabut, K. Jeamjumnunja, C. Prasittichai and W. Siriwatcharapiboon, *ACS Appl. Nano Mater.*, 2024, **7**, 267–278.

53 S. Bunnasit, K. Thamsirianunt, R. Rakthabut, K. Jeamjumnunja, C. Prasittichai and W. Siriwatcharapiboon, *ACS Appl. Nano Mater.*, 2024, **7**, 267–278.

54 C. Chen, Y. Liu, C. Liang, H. Li, Z. Wan, H. Xiao, J. Wang, J. Liu, G. Deng and M. Yang, *J. Food Compos. Anal.*, 2024, **129**, 106114.

55 S. Golczak, A. Kanciurzewska, M. Fahlman, K. Langer and J. J. Langer, *Solid State Ionics*, 2008, **179**, 2234–2239.

56 T. Van Tran, D. T. C. Nguyen, H. T. N. Le, L. G. Bach, D. V. N. Vo, S. S. Hong, T. Q. T. Phan and T. D. Nguyen, *Nanomaterials*, 2019, **9**, 237.

57 T. Lai, H. Shu, B. Yao, S. Lai, T. Chen, X. Xiao and Y. Wang, *Biosensors*, 2023, **13**, 505.

58 W. Zhang, Z. Zhang, Y. Li, J. Chen, X. Li, Y. Zhang and Y. Zhang, *Sens. Actuators B Chem.*, 2017, **247**, 756–764.

59 J. Rafi, M. Daniel and B. Neppolian, *Chemosphere*, 2024, **357**, 141981.

60 T. Lai, H. Shu, B. Yao, S. Lai, T. Chen, X. Xiao and Y. Wang, *Biosensors*, 2023, **13**, 505.

© 2026 The Author(s). Published by the Royal Society of Chemistry

Environ. Sci.: Adv., 2026, **5**, 1162–1173 | **1173**